The Mid-infrared Instrument for JWST and Its In-flight Performance

Gillian Wright, George Rieke, Alistair Glasse, Michael Ressler, Macarena García Marín, Jonathan Aguilar, Stacey Alberts, Javier Álvarez-Márquez, Ioannis Argyriou, Kimberly Banks, et al.

CrossMark

The Mid-infrared Instrument for JWST and Its In-flight Performance

Gillian S. Wright[1], George H. Rieke[2], Alistair Glasse[1], Michael Ressler[3], Macarena García Marín[4],
Jonathan Aguilar[5], Stacey Alberts[2], Javier Álvarez-Márquez[6], Ioannis Argyriou[7], Kimberly Banks[8], Pierre Baudoz[9],
Anthony Boccaletti[9], Patrice Bouchet[10], Jeroen Bouwman[11], Bernard R. Brandl[12], David Breda[3], Stacey Bright[5],
Steven Cale[8], Luis Colina[6], Christophe Cossou[13], Alain Coulais[14], Misty Cracraft[5], Wim De Meester[15], Daniel Dicken[1],
Michael Engesser[5], Mireya Etxaluze[16], Ori D. Fox[5], Scott Friedman[5], Henry Fu[17], Danny Gasman[15],
András Gáspár[2], René Gastaud[10], Vincent Geers[1], Adrian Michael Glauser[18], Karl D. Gordon[5], Thomas Greene[19],
Thomas R. Greve[20], Timothy Grundy[16], Manuel Güdel[21], Pierre Guillard[22], Peter Haderlein[3], Ryan Hashimoto[17],
Thomas Henning[11], Dean Hines[5], Bryan Holler[5], Örs Hunor Detre[11], Amir Jahromi[8], Bryan James[8], Olivia C. Jones[1],
Kay Justtanont[23], Patrick Kavanagh[24], Sarah Kendrew[4], Pamela Klaassen[1], Oliver Krause[11], Alvaro Labiano[6],
Pierre-Olivier Lagage[25], Scott Lambros[8], Kirsten Larson[26], David Law[5], David Lee[1], Mattia Libralato[26],
Jose Lorenzo Alverez[27], Margaret Meixner[28], Jane Morrison[2], Migo Mueller[29], Katherine Murray[5], Matthew Mycroft[3],
Richard Myers[17], Omnarayani Nayak[5], Bret Naylor[3], Bryony Nickson[5], Alberto Noriega-Crespo[5], Göran Östlin[30],
Brian O'Sullivan[4], Richard Ottens[8], Polychronis Patapis[18], Konstantin Penanen[3], Martin Pietraszkiewicz[17], Tom Ray[24],
Michael Regan[5], Anthony Roteliuk[17], Pierre Royer[15], Piyal Samara-Ratna[31], Bridget Samuelson[17], Beth A. Sargent[5],
Silvia Scheithauer[11], Analyn Schneider[3], Jürgen Schreiber[11], Bryan Shaughnessy[16], Evan Sheehan[8], Irene Shivaei[2],
G. C. Sloan[5], Laszlo Tamas[1], Kelly Teague[5], Tea Temim[32], Tuomo Tikkanen[31], Samuel Tustain[16], Ewine F. van Dishoeck[12],
Bart Vandenbussche[15], Mark Weilert[3], Paul Whitehouse[8], and Schuyler Wolff[2]
[1] UK Astronomy Technology Centre, Royal Observatory Edinburgh, Blackford Hill, Edinburgh EH9 3HJ, UK
[2] Steward Observatory, The University of Arizona, Tucson, AZ, 85750, USA; grieke@as.arizona.edu
[3] Jet Propulsion Laboratory, California Institute of Technology, 4800 Oak Grove Drive, Pasadena, CA, 91109, USA
[4] European Space Agency, at Space Telescope Science Institute, 3700 San Martin Drive, Baltimore, MD, 21218, USA
[5] Space Telescope Science Institute, 3700 San Martin Drive, Baltimore, MD, 21218, USA
[6] Centro de Astrobiología (CAB, CSIC-INTA), Carretera de Ajalvir, E-28850 Torrejón de Ardoz, Madrid, Spain
[7] Institute of Astronomy, KU Leuven, Celestijnenlaan 200D, B-3001 Leuven, Belgium
[8] NASA Goddard Space Flight Center, 8800 Greenbelt Road, Greenbelt, MD 20771, USA
[9] LESIA, Observatoire de Paris, Université PSL, CNRS, Sorbonne Université, Université de Paris, 5 place Jules Janssen, F-92195 Meudon, France
[10] Laboratoire AIM Paris-Saclay, CEA-IRFU/SAp, CNRS, Université Paris Diderot, F-91191 Gif-sur-Yvette, France
[11] Max Planck Institute for Astronomy, Königstuhl 17, D-69117 Heidelberg, Germany
[12] Leiden Observatory, Leiden University, PO Box 9513, 2300 RA Leiden, The Netherlands
[13] Université Paris-Saclay, CEA, Département d'Electronique des Détecteurs et d'Informatique pour la Physique, F-91191, Gif-sur-Yvette, France
[14] LERMA (CNRS) & Observatoire de Paris, Paris, France
[15] Instituut voor Sterrenkunde, KU Leuven, Celestijnenlaan 200D, Bus-2410, B-3000 Leuven, Belgium
[16] RAL Space, STFC, Rutherford Appleton Laboratory, Harwell, Oxford, Didcot OX11 0QX, UK
[17] Northrop Grumman Aerospace Systems, One Space Park, Redondo Beach, CA 90278, USA
[18] ETH Zurich, Institute for Particle Physics and Astrophysics, Wolfgang-Pauli-Str 27, CH-8093 Zurich, Switzerland
[19] NASA Ames Research Center Space Science and Astrobiology Division M.S. 245-6 Moffett Field, CA 94035, USA
[20] DTU Space, Technical University of Denmark. Building 328, Elektrovej, DK-2800 Kgs. Lyngby, Denmark
[21] Dept. of Astrophysics, University of Vienna, Türkenschanzstr 17, A-1180 Vienna, Austria
[22] Sorbonne Universites, UPMC Paris 6 et CNRS, UMR 7095, Institut dAstrophysique de Paris, 98 bis Bd Arago, F-75014 Paris, France
[23] Dept. of Space, Earth and Environment, Chalmers University of Technology, Onsala Space Observatory, SE-43992 Onsala, Sweden
[24] Dublin Institute for Advanced Studies, School of Cosmic Physics, 31 Fitzwilliam Place, Dublin 2, D02 XF86, Ireland
[25] Université Paris-Saclay, Université de Paris, CEA, CNRS, AIM, F-91191 Gif-sur-Yvette, France
[26] AURA for the European Space Agency (ESA), Space Telescope Science Institute, 3700 San Martin Drive, Baltimore, MD 21218, USA
[27] ESTEC, Keplerlaan 1, 2201 AZ Noordwijk, The Netherlands
[28] SOFIA-USRA, NASA Ames Research Center, MS 232-12, Moffett Field, CA 94035, USA
[29] Kapteyn Astronomical Institute, University of Groningen, P.O. Box 800, 9700 AV Groningen, The Netherlands
[30] Department of Astronomy, Oskar Klein Centre; Stockholm University; SE-106 91 Stockholm, Sweden
[31] School of Physics & Astronomy, Space Research Centre, University of Leicester, Space Park Leicester, 92 Corporation Road, Leicester LE4 5SP, UK
[32] Princeton University, 4 Ivy Lane, Princeton, NJ 08544, USA

1

Abstract

The Mid-Infrared Instrument (MIRI) extends the reach of the James Webb Space Telescope (JWST) to 28.5 μm. It provides subarcsecond-resolution imaging, high sensitivity coronagraphy, and spectroscopy at resolutions of $\lambda/\Delta\lambda \sim 100$–3500, with the high-resolution mode employing an integral field unit to provide spatial data cubes. The resulting broad suite of capabilities will enable huge advances in studies over this wavelength range. This overview describes the history of acquiring this capability for JWST. It discusses the basic attributes of the instrument optics, the detector arrays, and the cryocooler that keeps everything at approximately 7 K. It gives a short description of the data pipeline and of the instrument performance demonstrated during JWST commissioning. The bottom line is that the telescope and MIRI are both operating to the standards set by pre-launch predictions, and all of the MIRI capabilities are operating at, or even a bit better than, the level that had been expected. The paper is also designed to act as a roadmap to more detailed papers on different aspects of MIRI.

Unified Astronomy Thesaurus concepts: Space vehicle instruments (1548); Astronomical instrumentation (799)

1. Introduction

The Mid-Infrared Instrument (MIRI) for JWST provides a huge advance for mid-infrared (5–28.5 μm) astronomy. This spectral range is severely limited in sensitivity from the ground due to intense emission by the telescope and the atmosphere of the earth. This foreground emission is of the order of 10^9 photons s^{-1} into a diffraction-limited field of view (FOV) at the full N band (10 μm). It severely limits the sensitivity to faint sources. Methods have been developed to detect them at 10 and 20 μm down to about 1/100,000 of the total flux on the detector, and this statistic by itself illustrates the challenge.

The most sensitive imaging and moderate-resolution spectroscopy in this range have depended on a series of cold telescopes in space—the Infrared Astronomical Satellite, the Infrared Space Observatory, the Spitzer Space Telescope, Akari, and the Wide-field Infrared Survey Explorer. Although each of these missions brought significant improvements in sensitivity and/or sky coverage, none of them had a telescope aperture as large as 1 m; as a result, they were all severely limited in angular resolution by diffraction. Mid-infrared instruments on ground-based telescopes—e.g., CanariCam on the Gran Telescopio CANARIAS, the Large Binocular Telescope Interferometer, MICHELLE on GEMINI, and VISIR on the VLT—provide high spatial and spectral resolution but at greatly reduced sensitivity. The gain in clarity with the subarcsecond MIRI beam across the entire mid-IR is just as large a revolution as is its improved sensitivity, as shown in Figure 1.

Nonetheless, the sensitivity of MIRI is equally important. The sensitivity of JWST is limited by the natural background (i.e., zodiacal emission) from 5 to at least 12.5 μm (see Rigby et al. 2023). Over this range, the MIRI detection limits scale from those of Spitzer as the relative apertures squared (assuming a diffraction-limited beam in both cases), that is, as a factor of about 50. One might expect a smaller (or even no) gain at the longer wavelengths where MIRI has to contend with the emission of the 40 K telescope while Spitzer was cold

enough to be natural background limited. However, the comparison is not that simple. For short exposures the conclusion is more or less correct, but the lower spatial resolution of MIPS on Spitzer results in it becoming limited by confusion noise at which point the much smaller point-spread function (PSF) with MIRI starts to make up the potential difference. Dole et al. (2004) derived that the 5σ confusion limit for MIPS at 24 μm is 56 μJy. Taking 11 μJy as the 1σ confusion flux density, MIRI reaches this level for a point source at 21 μm in about 1500 s and in exposures longer than this value can go deeper than is possible with MIPS. Correcting for the actual aperture of JWST, Dole et al.'s (2004) estimate of its confusion limit is about 0.27 μJy at these wavelengths. Reaching the 5σ level at this flux density with MIRI at 21 μm requires about 150 hr of integration, i.e., MIRI will virtually never be seriously limited by confusion noise and will obtain extremely deep exposures of unbiased sky.

Previous missions with mid-infrared spectrographs and the spectrographs on 8 m class ground-based telescopes have demonstrated the rich astrophysics from spectroscopy at these wavelengths, but were limited in resolution, sensitivity, and by the atmosphere. The large aperture of JWST combined with advances in detector formats allows a sophisticated integral field medium-resolution spectroscopy capability to be provided in space for the first time at these wavelengths. An example of the applications is to use the neon fine structure lines to determine the excitation mechanism of emission line objects, e.g., distinguishing excitation by active galactic nuclei from that by hot stars, and also identifying excitation by very hot (i.e., Wolf–Rayet) stars versus hot main-sequence ones. Other than the [Ne II] 12.8 μm line, all of these lines are blocked by atmospheric absorption: [Ne III] 15.56 μm, [Ne V] 14.32 μm, and [Ne VI] 7.64 μm. Another example is that the interstellar silicate broad absorptions at $\sim$10 and 18 μm align with the N- and Q-band atmospheric windows—the interstellar windows at $\sim$7 and 15 μm are in anticoincidence with the atmospheric windows. Thus, penetrating cold cloud cores and other heavily
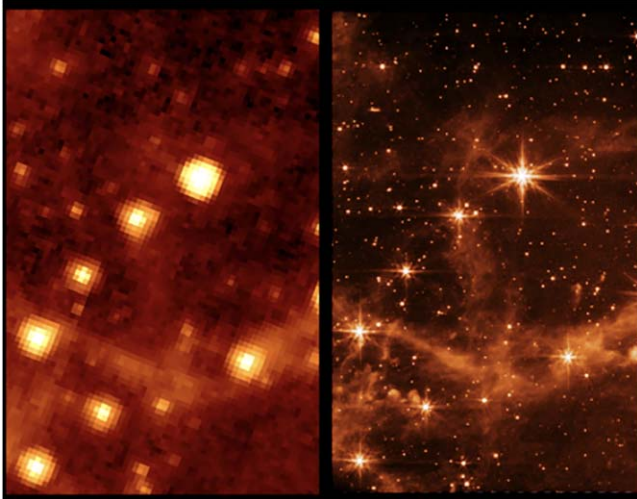
Figure 1. Comparison of the same field imaged with IRAC on Spitzer at 7.8 μm (left) and MIRI at 7.7 μm (right). The field is about $70'' \times 111''$ in size. Figure courtesy of András Gáspár.

obscured environments can be done much more thoroughly from space than from the ground (e.g., van Dishoeck 2004).

The result of these gains is that MIRI on JWST will be unsurpassed in imaging and spectroscopy not only now but for the foreseeable future. It will fill the archive with data that the astronomical community will draw upon for decades. Among other applications, these data will provide the foundation for programs of mid-infrared studies with existing large ground-based telescopes and the coming generation of giant ones. The strengths of those telescopes will be ultra-high angular resolution and higher spectral resolution. The current emphasis is on the immediate science return from MIRI. However, MIRI will also leave a legacy that will underpin and motivate future studies in many forms, including those enabled by giant telescopes.

2. Origins of MIRI

JWST originated from the challenge by Riccardo Giacconi to develop an ambitious telescope concept to build on the Hubble Space Telescope. Technical development toward a 6 m version was endorsed in the American 1990 decadal survey (Illingworth 2016; Mather et al. 2023). The initial thermal study (Bely et al. 1987) projected that "A mirror temperature of 130 K or less appears to be obtainable by purely passive means." In follow up studies, the emphasis was on the near-infrared, both from technical considerations (e.g., the telescope temperature and achieved detector performance at the mid-infrared wavelengths) and because of the emphasis on detecting "first light" and other programs related to an "origins" theme. Nonetheless, it was recommended to extend the response "longward to about 20 μm, as far as is technically possible and

cost effective" (Dressler et al. 1996). In the 2000 decadal survey, the planned wavelength range was listed as 0.6–10 μm with a minimum of 1–5 μm and a goal of 0.6–20 μm (McKee et al. 2001). By then, steps were underway both in Europe and in the US to provide such an instrument, if practicable. Two advances had helped establish the feasibility of a high-performance mid-infrared instrument: the development of the Spitzer Space Telescope had demonstrated approaches for passive cooling to ~40 K (later confirmed in flight) and had advanced mid-infrared detector array performance substantially. In addition to imaging, theoretical work predicted substantial advances would be achieved with mid-infrared spectroscopy (e.g., Hollenbach & McKee 1989; Spinoglio & Malkan 1992), which was starting to be confirmed from the ground and by platforms such as the Kuiper Airborne Observatory and particularly by the Infrared Space Observatory. There was thus a strong scientific and technical case for an instrument combining imaging and spectroscopy.

NASA and ESA agreed to support the development of an instrument with the basic parameters of MIRI, and for the development to be split with ESA supplying the optical system and the US the data chain and software. A consortium had been formed under ESA sponsorship in which 10 member state national space agencies funded the development by the consortium institutes. The effort was led by the UK Astronomy Technology Centre with management and technical support through EADS Astrium (now Airbus). At that point, the cooling was to be via a liquid hydrogen cryostat supplied by ESA, but the responsibility for this component was transferred to the US at the time ESA agreed to supply the launch vehicle and the division of responsibilities between Europe and the US was finalized. To solve problems with mass and center of gravity in the observatory, following the preliminary design reviews, the cryostat was replaced with a mechanical cooler in 2005 (Banks et al. 2008). This change completed the basic MIRI concept that was taken into detailed design and construction.

3. MIRI Design and Performance

Since MIRI is the only instrument on JWST operating beyond 5 μm, it combines a broad range of science functions into a compact overall instrument: (1) standard imaging; (2) high-contrast (coronagraphic) imaging; (3) low-resolution spectroscopy with and without a slit; and (4) medium-resolution integral field unit (IFU) spectroscopy. These functions are combined in an all-aluminum optical system as illustrated in Figure 2 and implemented as in Figure 3. While the observing modes are optically distinct, the instrument design uses common features such as diamond-turned optical surfaces, coatings, calibration sources, mechanisms, structure, focal plane interfaces, and thermal design. To avoid compromising performance, the instrument itself needs to be at <16 K,
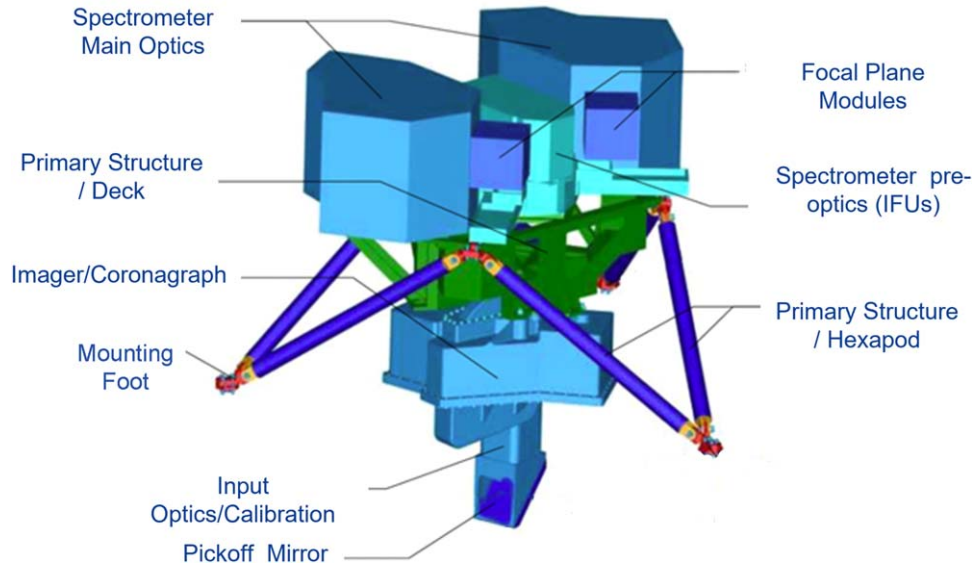
Figure 2. A solid model rendering of the MIRI optomechanical system without its cryocooler. Three mounting feet attach the deck through the hexapod struts to the JWST Integrated Science Instrument Module (ISIM) conductive interface, which is at ∼40 K. The MIRI instrument components are suspended off this deck. The entire optics module (OM) shown is surrounded by a radiation shield (not shown). Image credit: P. Samara-Ratna.
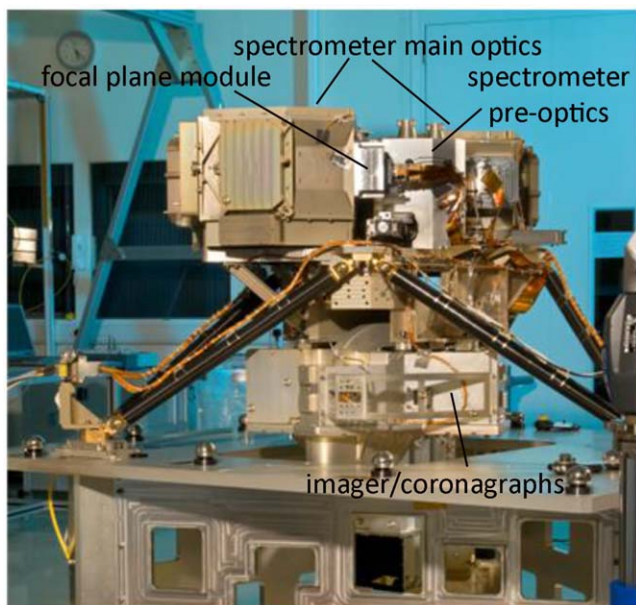

Figure 3. The MIRI Flight Model prior to delivery. The OM structure is aluminum; the hexapod truss that mounts it to the telescope is black carbon fiber reinforced plastic. Image credit: STFC/RALSpace.

while to control dark current, the detectors need to be at <7 K. The adopted approach is to use a cryocooler (Section 4) to cool both detectors and optical bench to a similar temperature, but with the detectors thermally isolated from the bench and connected to a dedicated heat sink. This design allows the detectors to be heated slightly above the heat sink temperature

so that their operating temperature can be stabilized. The optics are thermally isolated from the Integrated Science Instrument Module (ISIM) by the carbon fiber hexapod seen in the two figures and radiatively isolated by a Multi-Layer Insulation (MLI) blanket and a thermal shield. The MLI was optimized for low-temperature operation by reducing the number of layers and making them thicker. Heat loads from the instrument required careful engineering, for example, by minimizing the number of mechanisms with a design that, unlike the near-infrared instruments, has no focus mechanism or decontamination heaters, and by close attention to signal and command harnesses redundancy. The Input Optics and Calibration module contains a contamination control cover that successfully protected MIRI from ice deposition during the JWST cool-down sequence. We describe each optically distinct observing mode and summarize key aspects of the achieved performance below; Table 1 provides a list of relevant design references.

3.1. Imager

The design of the MIRI imager is described in Bouchet et al. (2015), and details of the performance are presented in D. Dicken et al. (2023, in preparation). The imager optics consists of an ellipsoidal mirror to form a pupil for the imager filters and cold stops, a fold mirror, and then a three-mirror anastigmat. The image scale is $0\rlap{.}''11$ per pixel, which is slightly undersampled relative to the Nyquist criterion at the shortest wavelengths but satisfies the criterion at 6.25 μm and longer wavelengths. To provide the coronagraph and low-resolution

Topic	Reference[a]
Overall design	*Wright et al.* (2015), Renouf & Wright (2006)
Imager	*Bouchet et al.* (2015), Amiaux et al. (2008)
Coronagraphs	*Boccaletti et al.* (2015), *Boccaletti et al.* (2022), Baudoz et al. (2006), Rouan et al. (2007), Lajoie et al. (2014)
Low Resolution Spectrometer	*Kendrew et al.* (2015), Fischer et al. (2008), Rossi et al. (2008), Bouchet et al. (2022)
	Kendrew et al. (2016), Kendrew et al. (2018)
Medium Resolution Spectrometer	*Wells et al.* (2015), Glauser et al. (2010), Kroes et al. (2010), Argyriou et al. (2020), Labiano et al. (2021)
Filter wheel mechanisms	*Krause et al.* (2008)
Cooler	*Durand et al.* (2009), Ross et al. (2004), Banks et al. (2008), Penanen et al. (2020)
Thermal Design	*Shaughnessy* (2012)

Note.
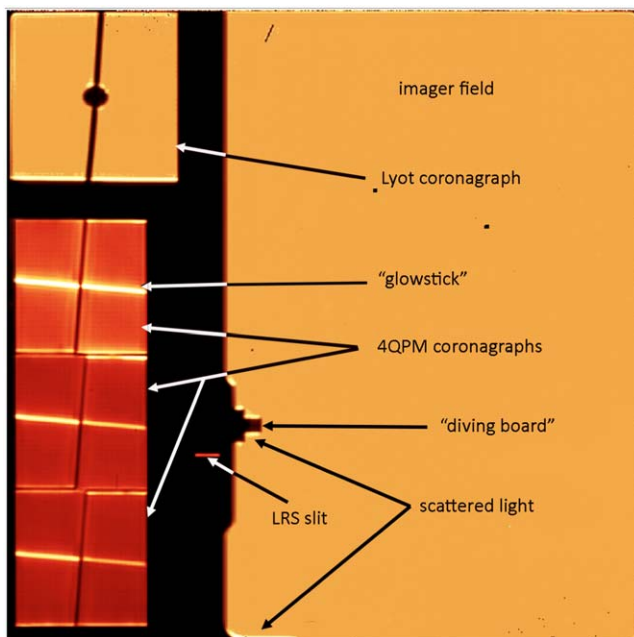[a] Primary references are given in italics.

Figure 4. Layout of the MIRI imager FOV. The figure also shows the observatory scattered light as seen by the MIRI imager in the F2550W filter, around the "diving board," the bottom rows, and the coronagraphs (e.g., the glowsticks). Image credit: M. García Marín.
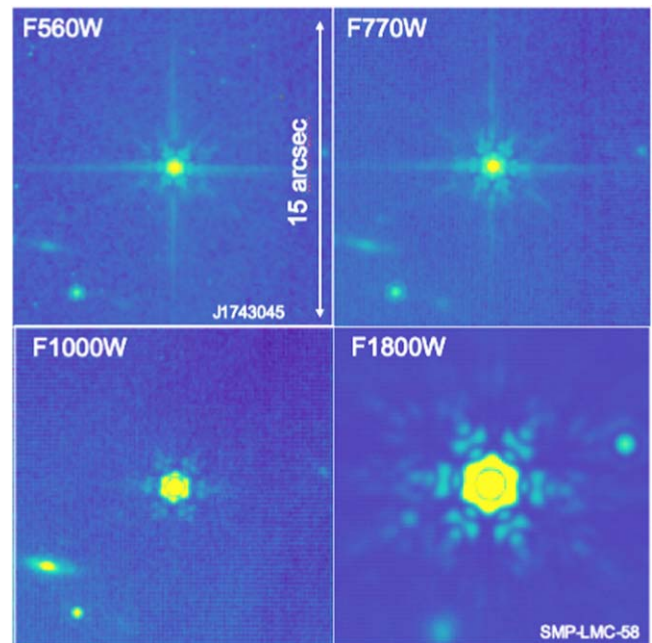

Figure 5. PSF stamps from flat-fielded images. We show three log-scale, 15″ cropped images of 2MASS J17430448 + 6655015 and, at the bottom right, the planetary nebula SMP-LMC-58. Image credit: P. Guillard.

spectroscopy functions without additional mechanisms, a part of the 1024×1024 pixel array is dedicated to these functions (see Figure 4). This gives a clear imager FOV of $74'' \times 113''$. Imaging can also be conducted in subarrays, e.g., to avoid saturation by bright sources. There are eight broadband filters, providing bands starting at 5.6 μm and spaced every factor of $\sim$1.2–1.3 to 25.5 μm, with bandwidths of $\Delta\lambda/\lambda \sim 0.2$. An additional 6% bandwidth filter is centered on the aromatic feature at 11.3 μm. Specific center wavelengths and passbands are provided in Bouchet et al. (2015), and throughputs can be

obtained from the documentation of the JWST Exposure Time Calculator (ETC).

The imager is diffraction limited over its full wavelength range; the total wave front error is 0.02–0.03 λ rms at 5.6 μm, with contributions divided roughly equally between the telescope and the instrument optics. This indicates a nearly perfect Strehl ratio starting from the shortest wavelengths. The FWHM and encircled energies measured for all filters and field positions were determined to be within a few percent of expectations; sample images are shown in Figure 5. This result is due to a combination of the excellent performance of the

JWST telescope optics, meeting the required precision in MIRI mounting to the ISIM, and also the MIRI optics performance.

The thermal backgrounds from the telescope match the pre-launch predictions very closely and preserve the expected high sensitivity of MIRI (Rigby et al. 2023). The longer wavelength imager bands have a smooth but structured level of emission across the field that is not related to residual systematics from the flat-field correction, but is rather the background itself. It has been shown that these residuals can be removed using dithered exposures, allowing the background to be removed either by differencing, or by using a median filter technique if the size of the science target is larger than the offset induced by the dither pattern. Alternatively, independent background exposures can be used to remove the thermal telescope background.

All MIRI PSFs at wavelengths $\lesssim 10$ μm, show additional spikes in the vertical and horizontal directions in the instrument coordinate frame, called the "cruciform artifact." They can be seen in the frames for F560W and F770W in Figure 5. They are due to diffraction that occurs within the detector substrate itself at the detector electrical contacts, as described in Section 5 and references therein. Models based on flight data are able to reproduce the cross artifact in detail including the field dependence.

Some scattered light originating in the observatory (temperature of about 120 K) is observed in the imager along the edges of the structure that separates the imager field from the coronagraphic fields; it is confined to a small number of rows and columns near the edge of this structure, particularly near the "diving board," and along the rows at the bottom of the detector (lowest row numbers, i.e., toward the bottom in Figure 4). Because this light enters off the telecentric angles, it is removed by the internal stops, e.g., the pupil stop, and is only seen where structure in the physical focal plane of the instrument scatters it into the range of angles that pass the internal stray light rejection. The stray light observed at the edges of structures in the imager focal plane is not regarded as having any significant impact on imaging science performance.

The commissioning results confirm that the MIRI imager is working up to pre-launch expectations. Distortion measurements confirm the optical model. The imaging photometric stability was investigated with observations of two spectro-photometric standards BD+60 1753 and J1743045 (PID 1027; Gordon et al. 2022), which were observed twice with a separation of over a week. All photometric measurements (80% encircled energy) agreed to within 5%. Finally, MIRI imaging dither patterns were tested and function nominally, and are deemed essential for good performance. Observers are encouraged to consult the STScI documentation and, as needed, the instrument team, on optimum dither design for their science goals.

3.2. Coronagraphs

Four coronagraphs are placed along one side of the imager FOV, as described by Boccaletti et al. (2015; and see Figure 4). They operate at fixed wavelengths of 10.58, 11.30, 15.50, and 23 μm, with spectral bands of ~0.8 μm for the first three and 5.5 μm for the fourth (which also obtains images within its field that are provided to observers along with the combined images and mosaics from the main imager field). The longest-wavelength coronagraph is of conventional Lyot design with a central occulted stop of nearly 4 λ/D in radius. The three shorter wavelength units are based on four-quadrant phase masks (4QPMs) that have no physical central occulter; instead, the signal from a bright point source is canceled by interference when it is placed on the center of the wave plate, which is arranged to impose phase delays of π for one pair of diagonally opposite quadrants relative to the other. These latter units are capable of providing useful results for separations as small as λ/D, i.e., their inner working angles are almost as small as those of the conventional coronagraphs in NIRCam. However, because the phase plates are not achromatic, 4QPMs must operate over a relatively narrow spectral range.

On orbit, it was found that the stray light path at ~120 K described above impacts the calibration of coronagraph pointing offsets (to the null), and a new technique had to be developed. The coronagraphs are also the most prominent case of surfaces in the instrument focal plane that scatter some of the light from this path into a telecentric direction that allows it to get past the pupil stop. Consequently, the boundaries of the wave plate quadrants are lit up, creating what has been dubbed "glowsticks," as seen in Figure 4. Fortunately, now that the on-orbit location of the null has been measured accurately, the science impact is small because subtracting a reference image can remove this artifact with only a small noise impact on the coronagraphic data. Observers are currently required to obtain background observations to subtract to remove the glowsticks. We anticipate that in the future an accurate model will be developed to subtract this stray signal, which will reduce the small subtraction component to the noise and also improve operations efficiency.

The commissioning of the MIRI coronagraphs demonstrated performance surpassing that projected in Boccaletti et al. (2015) because of the excellent optical performance of the telescope and accurate MIRI alignment onto it; see Table 2. It was also shown that the 4QPM units are delivering the expected small inner working angle, validating the design decision to use them in MIRI so that similar inner working angles are available on JWST coronagraphs across the 1–15 μm range. The 4QPMs reach raw contrasts of $\lesssim 10^{-3}$ at small angular separations (~1″) and of 10^{-5} beyond ~6″ (Boccaletti et al. 2022). Commissioning directly tested the impact of slew size on PSF-subtracted contrast for MIRI coronagraphy, by using PSF reference stars located ~1° and ~10° from the target star. No significant difference in the final

Table 2
Coronagraph Achieved Contrast, after Boccaletti et al. (2022)

Coronagraph Unit	MASK1065	MASK1140	MASK1550	MASKLYOT
Raw contrast ($6\lambda/D$)	$10{,}570 \pm 240$	$12{,}700 \pm 330$	$14{,}700 \pm 480$	$10{,}260$
Rejection ($3\lambda/D$)	108.1 ± 8.8	108.8 ± 5.6	135.8 ± 7.1	233.5
With star subtraction ($3\,\sigma$ at $6\lambda/D$)	$61{,}800$	$47{,}300$	$24{,}100$	N/A
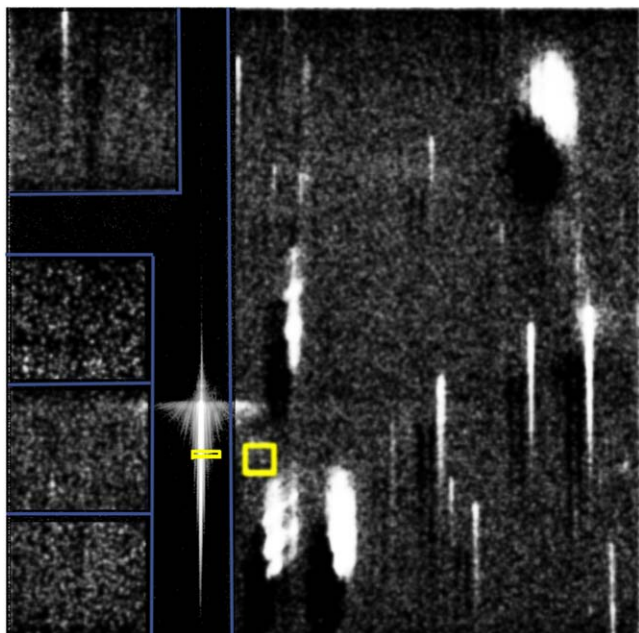
Figure 6. MIRI LRS data obtained during commissioning. To the left, the target source is placed on the slit (indicated by the narrow yellow rectangle) and dispersed; the horizontal feature is the cruciform artifact. The yellow box just left of center is the region of interest for target acquisition (TA). To the right, all sources present in the MIRI imager FOV are dispersed by the LRS in a "widefield slitless" mode. For the exoplanet transit slitless mode, the star is placed in the Lyot coronagraph field, to the upper left. Image credit: S. Kendrew.

PSF-subtracted contrast was observed for reference PSFs obtained sequentially with the science target.

The contrasts in Table 2 are achieved at the superior sensitivity of MIRI. Although significantly higher contrasts are obtained by modern coronagraphs from the ground, they are subject to the detection limits imposed by ground-based backgrounds. MIRI is unmatched in its potential to detect very faint sources and/or extended low surface brightness structures close to bright objects.

3.3. Low Resolution Spectrometer

The MIRI Low Resolution Spectrometer (LRS), described by Kendrew et al. (2015), performs as expected, and also benefits from the excellent image quality. The $0\rlap{.}''51$ wide by

$4\rlap{.}''7$ long entrance slit is placed in the supporting structure for the coronagraphs, between the 4QPM coronagraphs and the imaging field as shown in Figures 4 and 6. The spectral dispersion is achieved by a Ge/ZnS prism mounted on the imager filter wheel, designed so the Ge component cancels the deviation of the beam due to the ZnS disperser. Over most of the spectral range, the transmission of these prisms together is $\geqslant$80%, making the LRS ideal for obtaining spectra of very faint sources. The nominal spectral resolution is $R = \lambda/\Delta\lambda = 100$ at 7.5 μm, but varies linearly with wavelength from $R \sim 40$ at 4.5 μm to 160 at 10 μm. Although designed just for this spectral range, the commissioning data demonstrate useful throughput to $\sim$14 μm.

The relative calibrated spectral response for the LRS matches the spectrophotometric standard to better than 5% over the full 4.5–14 μm calibrated bandpass. The spectral calibration is affected by the placement of the target in the slit. The accuracy of target placement with target acquisition (TA) is around 10–15 mas along the detector y-axis, which is sufficient for achieving good wavelength calibration (see Figure 6 for the acquisition field). A TA verification image is often desirable to determine the position with high accuracy. Scattered light may contaminate the science spectrum, if a very bright target is found close to the science target (even if it is located behind the focal plane masking structure).

The LRS can also be operated in a slitless mode; in fact, when the prism is in the beam, the entire imager field provides slitless spectra (see Figure 6). The slitless mode has been optimized for observations of exoplanet transits. In this case, the source is placed toward one edge of the 23 μm coronagraph FOV, and the spectrum is read out as a subarray to provide maximum dynamic range. Obtaining spectra in slitless mode removes the possible modulation of the spectra due to image jitter at an entrance slit, and since for this science objective the target is a point source, there is no loss of spectral resolution. The spectra fold over at wavelengths short of $\sim$4.5 μm; this range is blocked by a filter at the slit for normal operation only; as a result, the short wavelengths of the spectra are contaminated in the slitless mode.

The MIRI LRS slitless time-series observation mode was tested during commissioning by observing a primary transit of the L168-9b (aka TOI-134) planet (Bouwman et al. 2023). This is a super-Earth orbiting a $K = 7.1$ (Vega) magnitude star with a period of 1.4 days and a transit time of 1.19 hr. The
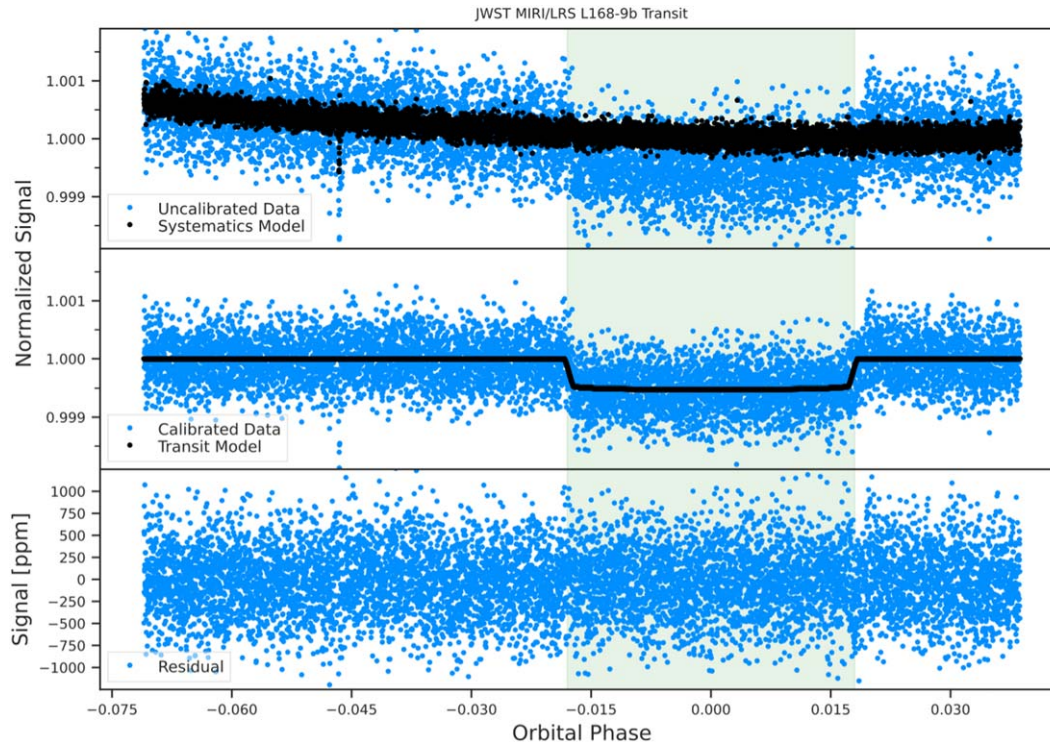
Figure 7. MIRI LRS slitless observation of a transit by exoplanet L168-9b. Top: white light curve with a model of the systematics (the first 20 minutes when the detector was settling have been removed). Middle: the systematic-corrected white light curve and the fitted transit model. Bottom: residuals after subtracting the transit model. Each point is an average of four integrations (∼6 s). Image credit: J. Bouwman.

observation is shown in Figure 7. The full exposure duration was 4.2 hr, covering a single transit with ample detector settling and out-of-transit time. The transit was easily recovered in the MIRI data, and the limiting spectrophotometric precision following our current best calibration is ∼25 ppm with R ∼50 at 7.5 μm and a spectrum to 11 μm. Initial detector settling time was approximately 20 minutes, during which a drift of ∼0.3% was seen in the detector response, after which the drift was much smaller (see Figure 7). Over the duration of the exposure, the pointing stability was extremely high (<0.1 pixel in both axes and limited by measurement precision). An extensive analysis of the MIRI LRS performance in this mode is provided in Bouwman et al. (2023); we note here simply that the achieved performance in this mode is better than anticipated, and provides a unique capability for the study of exoplanet atmospheres.

Extending the slitless capability to the full FOV, to support other science, may be possible in the future but suitable calibration methods will need to be developed. In any case, this would be a specialized mode since without a slit, the spectra have additional noise from the full background.

3.4. Medium Resolution Spectrometer

The Medium Resolution Spectrometer (MRS) is described in Wells et al. (2015). The choice of an IFU-based design for the

spectrometer was driven by both the scientifically valuable data cubes it provides for extended sources and a number of additional efficiency advantages: (1) the IFU captures light that would be lost in a conventional slit spectrometer without opening up the slit with a loss of spectral resolution; (2) the gratings can all be used in first order and near their blaze wavelengths; (3) the IFU slices can be adjusted in width to match the wavelength where they operate; and (4) for point sources, dithering only within the field of the IFU provides high observing efficiency. Structurally the MRS consists of the units labeled spectrometer pre-optics and spectrometer main optics in Figure 2, while the optical design is complex and integrated across them. Spectral resolutions of $\lambda/\Delta\lambda \gtrsim 2000$ for wavelengths shorter than 20 μm and $\lambda/\Delta\lambda \gtrsim 1500$ out to 28.5 μm were required to enable a wide range of spectroscopic studies.

In any spectrograph design with limited detector real estate, design decisions to distribute the available pixels between spatial and spectral information are needed. Two of the 1024×1024 pixel detector arrays were allocated to the MRS. The spectrum is divided into 12 subspectra, each with a dedicated grating used in first order for efficiency, and four image slicers are used to match the slice width to the broadening of the PSF as the wavelength increases. One image slicer per three subspectra defines the four main channels—
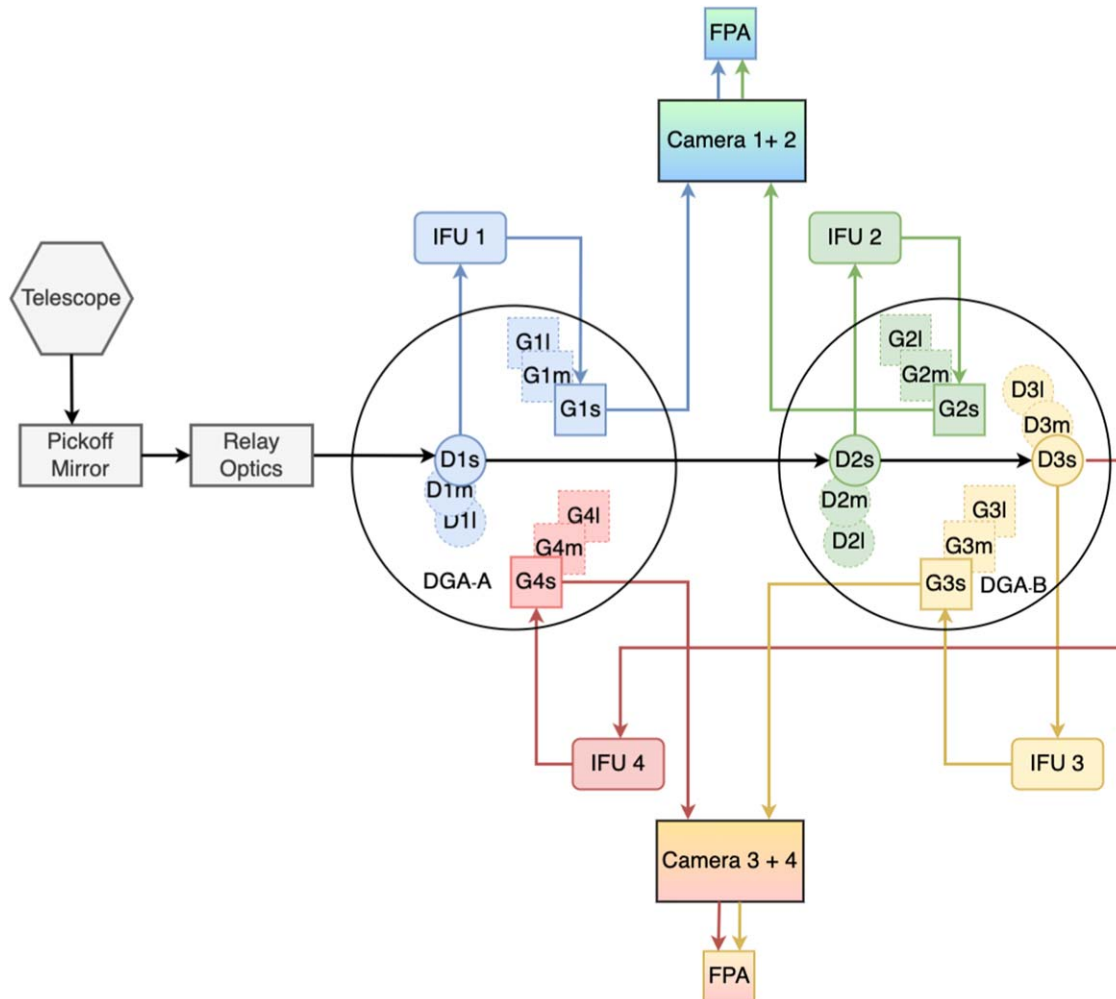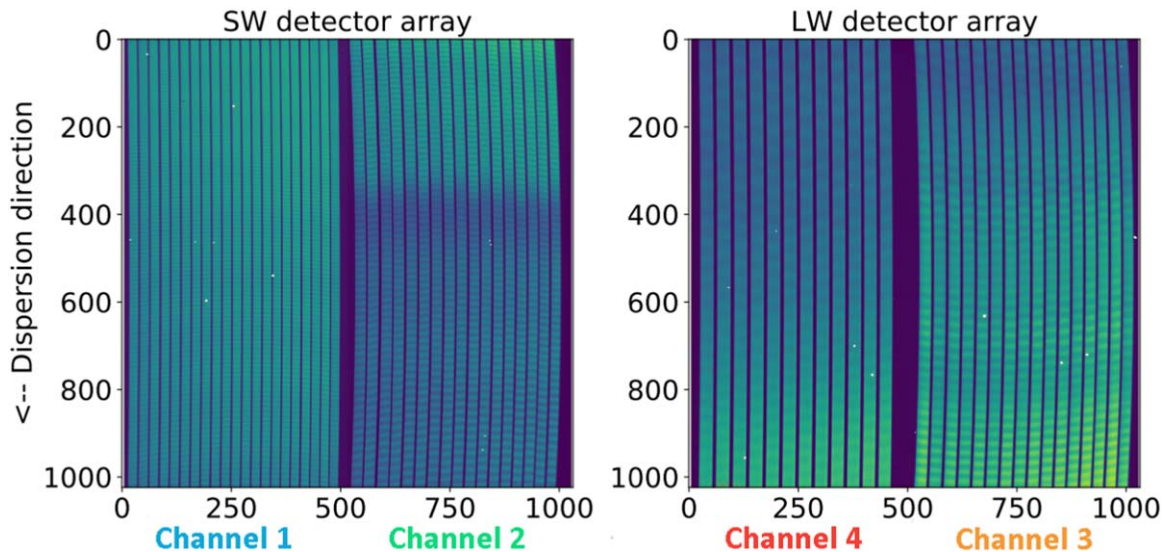
Figure 9. Result of a single exposure on the two detector arrays in the MRS. The illuminated bands correspond to IFU slices. Figure is from Argyriou et al. (2020).

means that at a single position of the mechanisms, four subspectra (one for each IFU) are measured simultaneously on the two detectors, as shown in Figure 9. DGA-A and DGA-B are then both rotated by 120° to bring the appropriate dichroics and gratings into play to obtain spectra for the medium subspectra (D1m, G1m, D2m, G2m, D3m, G3m, and G4m), and then again for the longest subspectrum (D1l, G1l, etc.) in each channel. This design provides very high observing efficiency, with a full spectrum nominally from 4.87–28.5 μm, requiring just three exposures.

A key design feature of mapping the IFU field onto the detector is the inclusion of nonilluminated rows between slices (as seen in Figure 9) and alternating the slices so that two neighboring slices "on the sky" are not neighboring on the detector. This design choice was made because it enabled the physical space to introduce a baffle for stray light control and it also aimed to facilitate calibration from the nonilluminated rows.

The bandwidths of the spectral channels were chosen such that the ratio $\lambda_{\rm long}/\lambda_{\rm short} = 1.54$. The overlap at the ends of the channel sub-bands allows accurate combination of the spectral segments. The IFUs are optimized for each channel, with a measured net FOV of $3{.}''2 \times 3{.}''7$ for the shortest to $6{.}''6 \times 7{.}''7$ for the longest (see Table 3). The gratings provide spectral resolutions of $\lambda/\Delta\lambda \sim 3000$ for wavelengths shorter than $\sim 11.7\,\mu$m, and 1500–2800, depending on wavelength, beyond $11.7\,\mu$m. A detailed description of the MRS performance compared to the design is provided in I. Argyriou et al. (2023, in preparation).

The FOVs of the IFUs and the spectral ranges of each channel and subchannel were measured during commissioning, and found to correspond well to the design expectation; see

Table 3. The wavelength calibration of the MIRI MRS data is generally accurate to within a fraction of a spectral resolution element throughout the MRS spectral range, and residual photometric offsets between subspectra are at the 2% level. These results are illustrated in Figure 10, showing a complete MRS spectrum of the B-type emission line star HD 76534. Calibration beyond 27.9 μm has not been achieved due to the very low signal throughput at these wavelengths, and crosstalk in the detector substrate (pull down; Dicken et al. 2022) with the much stronger signals in channel 3. Options to improve the detection of faint signals from very bright sources at $\lambda \gtrsim 27.9\,\mu$m may be developed in the future.

Scattered light occurring inside the detector substrate is an integral part of the MRS PSF. Inside the MRS detectors, light experiences multiple internal reflections between the detector antireflection coating and the pixel metalization. This "scattering" of photons causes the MRS PSF to be broader than the MRS optical design specifications and introduces a broad structured component to the signal. The PSF broadening is caused by the defocusing of the incoming beam as it scatters inside the thick MRS detector substrate. In addition, the cruciform (Figure 5) results in light deflected to large distances. The result of these effects is that part of the signal in one slice is detected in its neighboring slices. This is clearly visible in Figure 11, for the extended source illumination of Channels 1 and 2, where the signal does not drop to zero between the slices as expected from the optical design. Although less visible in Channel 2, the exact same issue arises for point-source illumination. Due to the shorter absorption length of the arsenic-doped silicon in Channel 3 and Channel 4, scattering is not an efficient pathway for the incoming photons, and the effect of the scattering becomes negligible at these longer
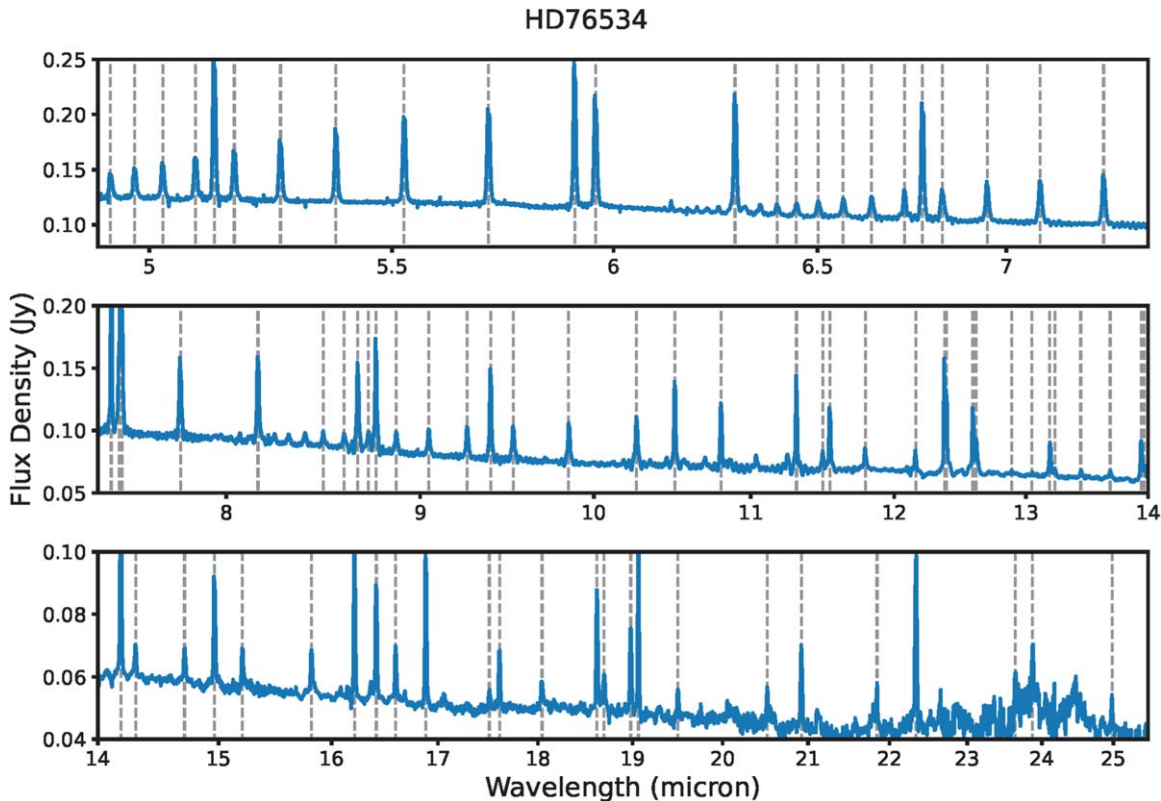
Figure 10. MIRI/MRS spectrum of the B-type emission line star HD 76534 (solid blue line). Dashed gray lines show the expected vacuum wavelengths of atomic hydrogen transitions corrected for the relative velocity of both the star and JWST with respect to the solar barycenter. The measured emission wavelengths match the expected values to within a fraction of a spectral resolution element throughout the MRS spectral range. Image credit: D. Law.

wavelengths. The PSF of point sources in the reconstructed images/data cubes fits accurately with the detector scattering model (Argyriou et al. 2021), and there is no evidence of other sources of scattered light between the slices.

The design decisions for the image slicer optics have proven extremely useful to identify the impact of the detector scattering on MRS spectra. They allowed for the development of an algorithm to remove the scattered light component from MRS data. Indeed, this was only possible due to knowing that, by design, if slice s contains a source, slices $s - 1$ and $s+1$ do not contain signals from that source, and hence the scattered light can be decoupled from the sky detector-projected radiometric field. A correction for the scattered light has been implemented in the current pipeline and reduces residuals from 20% of the total flux to 1%.

A few months after the start of science operations, an MRS grating move was halted due to excess friction. Following an in-depth investigation, a modified operations strategy was adopted to mitigate the issue, and the MRS has returned to normal operation.

An expected "feature" of the MRS spectra (Wells et al. 2015) is that they show strong fringing due to interference

effects and reflections off the internal structures, such as the buried contact. Work to predict, model, and remove the fringes is described in Argyriou et al. (2020, 2021). These large-amplitude sensitivity modulations with wavelength, in essence standing waves in the detector and in the dichroics, change across the MRS wavelength range. Amplitudes are highest at low wavelengths (up to 40% peak to peak). From channel 2C onward, there are multiple sources of significant fringing, and the fringe amplitude varies across the band due to beating between their contributions. On the long wavelength channels, we see an additional low-amplitude high-frequency modulation that is tentatively attributed to fringing within the dichroics. Two pipeline steps plus a post-pipeline notebook are available to correct for fringes. Taken together, they safely reduce the fringe contrast to below 6%, and further improvements are expected.

4. The MIRI Cooler

MIRI must operate at temperatures well below those that can be achieved by directly radiating heat into space, as other JWST instruments do. The MIRI operating temperature is provided with a mechanical cooler. The cooler design builds on
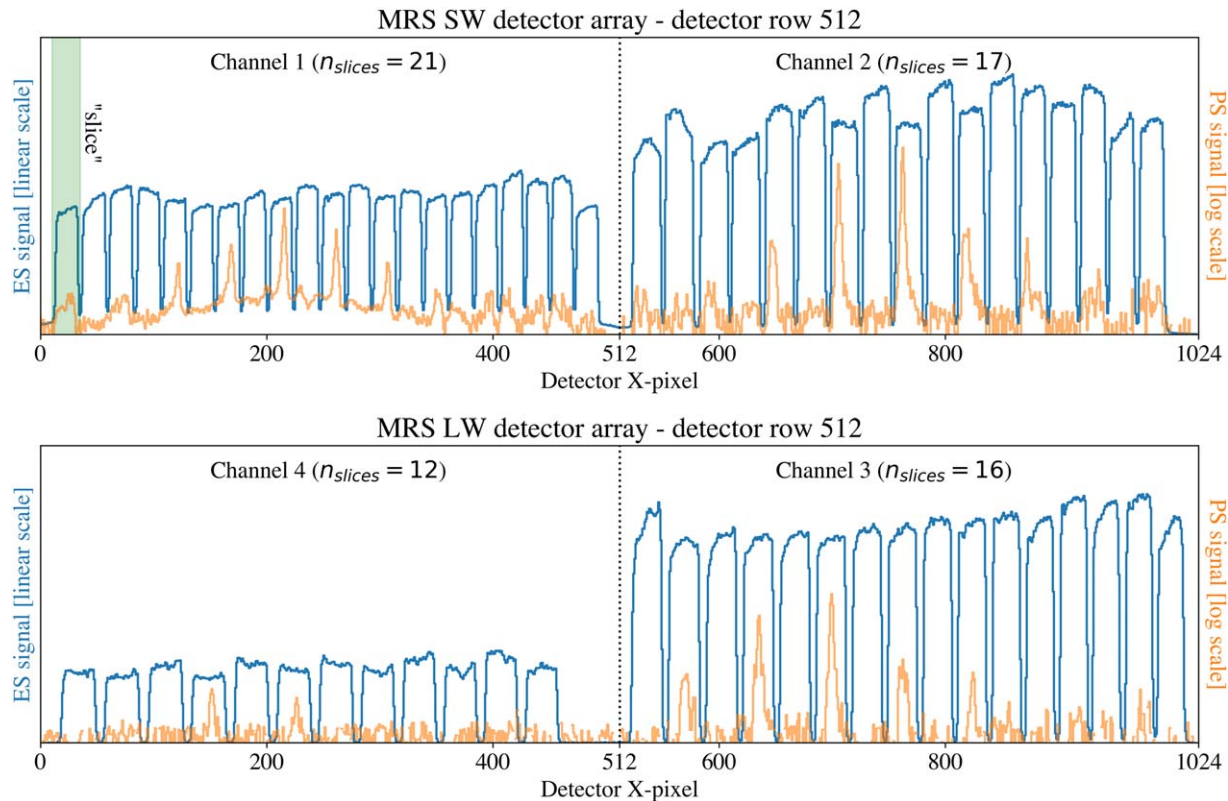
Figure 11. Measured MRS detector illumination, in one detector row, for an extended source (blue, linear scale) and point source (orange, log scale). Channels 1 and 2 are shown in the top panel, and Channels 3 and 4 are shown in the bottom panel. Each channel contains a different number of slices, where a "slice" is exemplified in one dimension by the green shaded area on the left of the top panel. For the extended source illumination (blue), the signal is measured for all slices in a channel. For the point-source illumination (orange), the telescope-plus-instrument PSF is split spatially by the image slicer. Different parts of the PSF are projected onto different parts of the detector in slices that do not neighbor one another, but alternate. Image credit: I. Argyriou.

a NASA investment in high-performance, low-temperature, spaceflight cryocoolers (Ross et al. 2004); the final design concept is described in Durand et al. (2009). It provides ⩾50 mW of heat lift from 6.2 K with 300 W of input power, a new benchmark for space-rated cryocoolers (Petach et al. 2018).

In this cooler, a pulse tube provides cooling to a bit below 20 K, and a Joule-Thomson constriction provides the final stage to achieve a temperature of ∼6 K. The pulse tube cooler works with an oscillating flow through a thermal matrix called a regenerator (a form of heat exchanger). In the high-pressure part of the cycle, gas is driven into a reservoir, where it loses energy to a heat exchanger. In the low-pressure part, the gas flows back through the regenerator and cools it. The final cooling stage starting from the ∼20 K achieved by the pulse tube cooler is to flow compressed helium through a constriction, where it expands and cools through the Joule-Thomson (J-T) effect.

Although straightforward in concept, realization of this approach required very careful thermal engineering. The cooler components are distributed over nearly the entire observatory, as shown in Figure 12. The control electronics, compressors,

and pulse tube stages reside in the spacecraft. Helium gas cooled by the pulse tube stages is piped through the refrigerant lines, including the refrigerant line deployable assembly, to the instrument. There it cools the optical bench and detectors to ∼6 K. On the return path, the helium cools the radiation shield around the MIRI optics to <30 K (Kimble et al. 2016), to reduce the load on the 6 K stage. The Optics Module (OM) is conductively isolated from the ISIM by the hexapod struts visible in Figure 3, which are attached to the ISIM conductive interface, having a temperature of about 40 K.

The heat lift provided by the pulse tube cooler decreases toward lower temperatures, while the heat lift by the J-T unit increases toward low temperatures. As a result, there is a minimum in available heat lift slightly below 20 K. Getting the OM to its operating temperature required that the cooler be able to transition through this "pinch point." Another requirement on the cooler is that the compressors be sufficiently well balanced and mechanically isolated that they would not cause pointing jitter for the telescope; this was done so successfully that the pointing jitter is indistinguishable whether the compressors are on or off. The cooler is operating very well
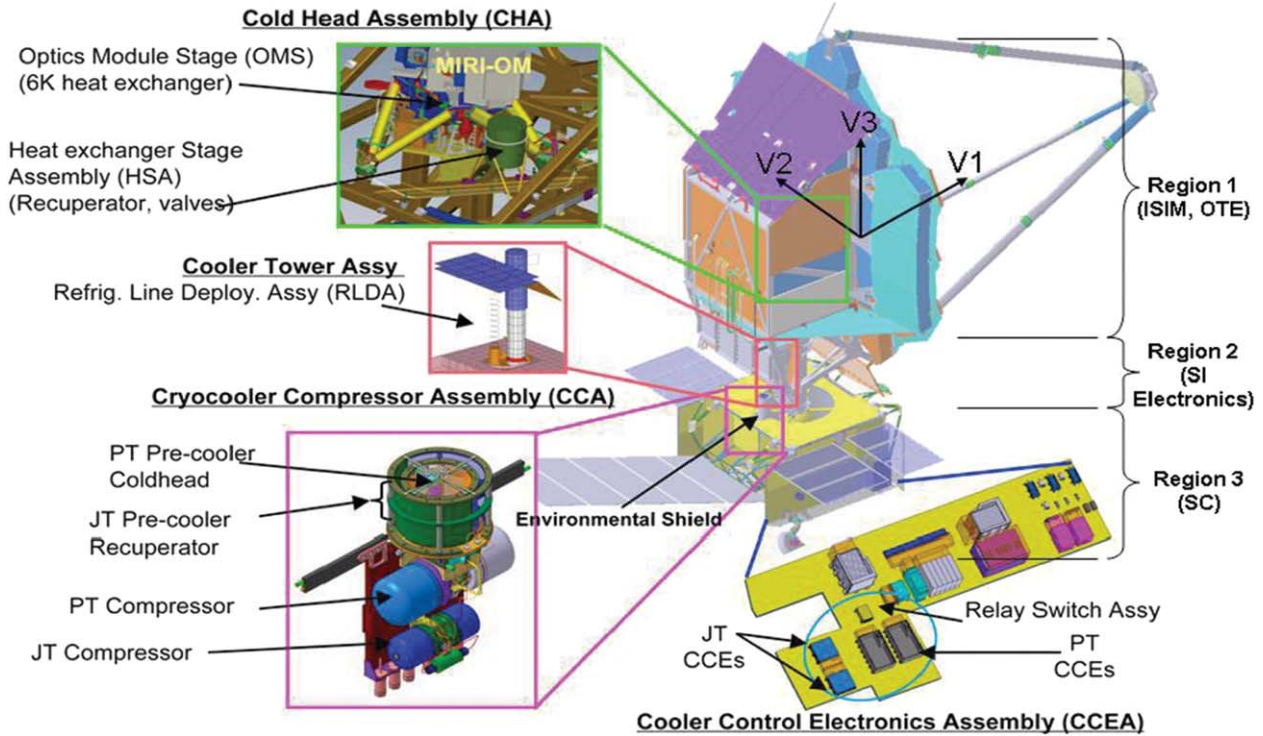
Figure 12. The MIRI cooler system. Region 1 is the telescope and ISIM, Region 2 is between them and the spacecraft, and Region 3 is the spacecraft bus itself.
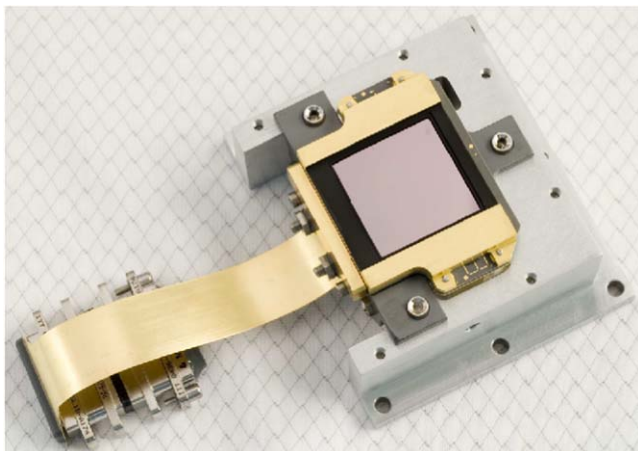

Figure 13. An MIRI focal plane assembly, provided by Raytheon Vision Systems.

and can be expected to provide cooling to MIRI for the entire duration of the JWST mission (Penanen et al. 2020).

5. MIRI Detector System

5.1. Focal Planes

MIRI uses arrays of 1024×1024 pixels of Si:As IBC (impurity band conduction) detectors (see Figure 13). This

detector type was invented by Petroff & Stapelbroek (1984) and provides some of the advantages of photodiodes, but in extrinsic material. The detector volume is divided into an infrared-absorbing layer so heavily doped that its impurity level spreads into a band. Between this layer and the output contact, there is a thin intrinsic layer. Only electrons that have been lifted into the conduction band by absorption of photons in the IR-active layer can penetrate the intrinsic layer to the output contact; thermally excited electrons within the impurity band are blocked at the intrinsic layer. Examples of the advantages over simple bulk photoconductors include: (1) the artifacts associated with dielectric relaxation in the high-impedance volume of a bulk photoconductor are eliminated; (2) high absorption efficiency can be achieved in a relatively small volume (important, for example, to minimize cosmic-ray effects); and (3) recombination noise is eliminated, i.e., for a given signal, the noise is $1/\sqrt(2)$ less. These detectors provide response from <5 to $\gtrsim 28\,\mu$m, with quantum efficiency (given suitable antireflection coatings) $\geqslant 40\%$ over the 5–26 μm band and $\geqslant 60\%$ over most of it (i.e., 7–24 μm). The read noise is $\leqslant 14$ electrons rms for Fowler-8 sampling (i.e., reading eight times and averaging). There is extensive heritage for use of these detectors in space astronomy missions, most directly in the case of MIRI with the detectors in the IRAC instrument on Spitzer (Wu et al. 1997; Hora et al. 2004), as discussed in Ressler et al. (2008) and Rieke et al. (2015). The excellent

Table 4
Studies and Analyses of MIRI Detector Behavior

Topic	Reference[a]
Detector and array architecture	*Ressler et al.* (2008, 2015), *Rieke et al.* (2015)
JPL characterization testing	*Sukhatme et al.* (2008), Bright et al. (2016)
Conversion of ramps to slopes, linearity corrections	*Morrison et al.* (2023)
Fringing	*Argyriou et al.* (2020, 2021)
Bias voltage and electron diffusion dependence of response	*Rieke et al.* (2015)
Quantum efficiency versus wavelength	*Gáspár et al.* (2021), Petroff & Stapelbroek (1984)
Latent images, persistence	D. Dicken et al. 2023, in preparation
Origin of cruciform artifact	*Gáspár et al.* (2021)
Reset anomaly, reset switch charge decay (RSCD)	Laine et al. 2023, in preparation
Pull-up/pull-down effects	*Dicken et al.* (2022)
Data chain	*Ressler et al.* (2015)
Data pipeline architecture	*Space Telescope Science Institute* (2023), Gordon et al. (2015), Labiano et al. (2016), Bright et al. (2017)
Cosmic-ray effects	*Hagan et al.* (2021), Glasse et al. (2020)

Note.
[a] Primary references are given in italics.

performance of IRAC is also characteristic of the devices in MIRI.

Nonetheless, the detectors show a number of artifacts in their data. To understand the detector behavior in depth, the MIRI team carried out an extensive series of characterization tests at the Jet Propulsion Laboratory, with plans for test objectives and reduction and interpretation of the test data spread across the entire team. In addition, the team has carried out extensive theoretical studies of the causes of these effects to improve the final products of data reduction. These studies are reported in the references listed in Table 4. The result of all of this work is that the MIRI data are virtually free of many artifacts arising from the detectors, with clean science products. Further information is in Morrison et al. (2023).

5.1.1. The Cruciform

A few detector effects are, however, unavoidable. One is the cruciform at the short wavelengths (5–10 μm). This type of effect occurs generally in detectors with poor absorption efficiency, which allows photons to traverse the absorption region and reflect from and be diffracted off the metallized output contacts. The purely reflected light can pass upward through the detector absorbing volume and exit near its point of entrance, increasing the absorption efficiency without significantly affecting the imaging. However, by Babinet's Principle, light will also be diffracted at the inter-pixel gaps and in this way can be bent to sufficiently large angles that the light is captured within the detector by total internal reflection. The result is a cross-shaped artifact on the MIRI images that can extend over many pixels (see Figure 5). This artifact can rival the traditional telescope diffraction pattern in prominence;

observers need to be aware of its influence on the PSF in the short wavelength (for MIRI) range.

5.1.2. Reset Switch Charge Decay

The MIRI detectors are read out by simple source follower amplifiers. If there is a significant signal on the integrating node of such amplifiers, it affects the space charge status in the channel of the reset field effect transistor. When the reset is completed and the switch is open, the resulting charge in the channel is injected into the integration node of the amplifier, reducing the detector bias; the amplifier recovers only slowly to the equilibrium bias (Yu 2010). As a result, the integration ramp is distorted—this is often called "the reset anomaly." We term this effect the "reset switch charge decay" (RSCD). The size of this residual charge scales with the size of the signal that is removed by the reset. To mitigate the effect, we carry out two resets at the start of each integration ramp. There are still small residual effects, so observers are recommended to obtain at least five groups (samples) up the integration ramp between resets, since this gives time for the integration ramp to settle close to its asymptotic value.

5.1.3. Latent Images

Like most infrared detectors, the MIRI devices show some degree of latent images or persistence after being exposed to a bright source. There are a number of suggestions for the cause. One possibility (private communication, "Dutch" Stapelbroek) is that the buried and output contacts with the intervening depleted high-impedance silicon in the IR-active and the intrinsic layers form a long time constant RC circuit. A large signal will partially debias the detector, changing the size of the depletion region in the IR-active layer, and when the signal is

removed, the detector relaxes back to its equilibrium state at this time constant. Another possibility is that there are traps at the buried contact. This structure is created by high-energy ion implantation to place it $\sim40\,\mu$m within the device, and the resulting crystal damage may not be fully removed by annealing. In any case, the latent images in the MIRI flight detectors are smaller than has been observed in other Si:As IBC devices (such as those in IRAC). Latent images from bright sources have been shown to dissipate to $<0.01\%$ of the imprinting source signal within 15–30 minutes. Nonetheless, they may appear in data that include exposures to extremely bright sources.

5.1.4. Pull-up/pull-down Effects

There is a form of electronic crosstalk, in which columns and rows with strong source signals can have their overall signal pulled up (a brightness increase) or down (a brightness decrease) in the flux image. The effect is flux dependent and manifests itself differently for rows than for columns. Further discussion can be found in Dicken et al. (2022).

5.1.5. Subarray Imprints

Operation in subarray mode can leave an artifact on the detector when it is returned to full-frame readout. This effect is mitigated operationally by always returning to full-frame readout after using a subarray.

5.1.6. Detector Annealing

Previous generations of Si:As IBC detectors have shown small drifts in characteristics, possibly the result of accumulated cosmic-ray damage. To clear any such effects and persistent latent images if they are found, the instrument has the capability to warm the focal planes to ~20 K, which thermalizes the detectors and erases most of the memory of past events. This cooler-assisted annealing can be used to remove latents and other detector artifacts if necessary; it has been verified to work during MIRI commissioning.

5.2. Data Chain

The MIRI detectors are controlled and their outputs received by warm electronics located in the ISIM Electronics Compartment, with a thermally isolating cable harness providing the necessary electrical connections. The detector outputs are digitized by conventional 16-bit analog/digital converters and packetized to be delivered to the ISIM Remote Services Unit where they are stored for later transmission to the ground.

The detectors are read out by sampling-up-the-ramp (MULTIACCUM), through four output amplifiers and at a rate of 10 μs per pixel. In full-frame mode, 2.775 s are required to read an entire detector array, while roughly proportionately faster read times are provided with subarrays. (There are some
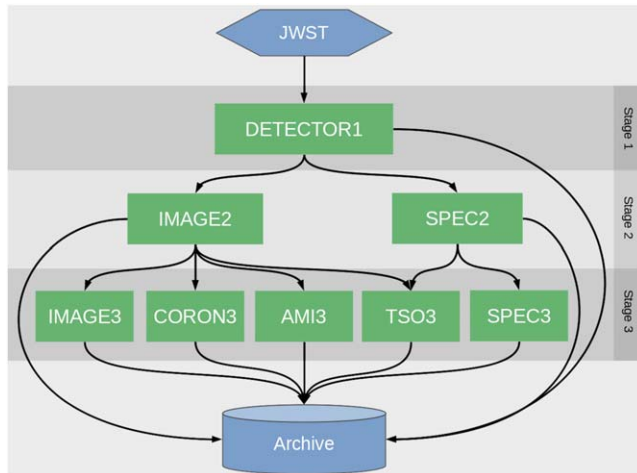

Figure 14. Overall flow of the JWST calibration pipeline. Credit: K. Gordon et al. (2023, in preparation).

readout overheads that prevent a pure scaling by area.) The samples are nondestructive, and normally all of the samples are sent to the ground. The standard terminology is that a "group" is a single, nondestructive read of all of the pixels in the array (a "frame" also describes a single read; for MIRI, there is only one frame per group in all readout modes, so the terms have the same meaning). An integration is defined as the time between the reset of the pixels (i.e., a destructive read). An exposure consists of one or more integrations.

6. Calibration Pipeline

The calibration pipeline has a shared architecture across all four JWST instruments (Figure 14), based on the following stages. Stage 1 of the pipeline carries out corrections to the detector outputs, on a group-by-group basis. Its product is an image generated by fitting the integration ramps for each exposure and correcting them to slopes with most detector artifacts removed and units of DN/s (Digital Numbers per second). Stage 2 carries out additional corrections and calibrations to produce fully calibrated exposures. Stage 3 includes processes for multiple exposures that generally produce some kind of combined product. Improvements in all three stages of the pipeline are expected as on-orbit data are accumulated. In any case, the relevant current documentation needs to be consulted carefully as part of understanding the pipeline products and any concerns about aspects of their performance, i.e., at the appropriate JWST website[33] and in K. D. Gordon et al. (2023, in preparation).

The MIRI team used this pipeline from its early inception, deriving algorithms from ground tests. Each step in the pipeline at all processing levels is defined by a calibration data product

---

[33] starting from https://jwst-docs.stsci.edu/.

or a set of parameters that capture the specific corrections for that step. Pre-launch, we used the MIRI simulator (MIRISim; Klaassen et al. 2021) both to model commissioning data and to cross check various pipeline steps. With this extensive preparation work, all commissioning data were analyzed using the pipeline. This approach facilitated rapid development of flight calibration and corrections to update the calibration data products, such that the pipeline products available to users are of publication quality from the start of operations, with known caveats that are well documented.[34]

The MIRI data pipeline (Morrison et al. 2023) begins Stage 1 with a quality check. Saturated pixels (if any) are identified; so far as possible, the signals are recovered by using just the initial, unsaturated portion of their integration ramps. Next, the first frame in an integration is rejected because it is affected by anomalies from the reset (even with the double reset). The last frame is then rejected; it is influenced by a signal coupled through the reset of the adjacent row pair and therefore shows anomalous offsets. The resulting ramps are corrected for nonlinearity pixel-by-pixel using the appropriate correction by wavelength. Next a correction is made for residual effects from the reset switch charge decay. Dark frames are subtracted and corrections to the ramps applied using the data from the reference pixels. Cosmic rays are identified through jumps in the integration ramps and the affected data are removed (this may be only part of the integration ramp). Finally, slopes are fitted to the corrected ramps and the resulting uncalibrated slope images are passed to stage 2.

Stage 2 processing results in a fully calibrated individual exposure. It includes steps such as: (1) assign world coordinate system information; (2) subtract background data (if appropriate); (3) apply flat-field corrections; (4) apply the photometric calibration; (5) resample as appropriate; and (6) for the spectrometers, following a point versus extended source decision, extract a one-dimensional spectrum. For the MRS, corrections are also applied for stray light and fringing, and a data cube is built. For time-series exposures, some steps are set to be skipped by default.

Examples of stage 3 products include: (1) the imaging routines combine calibrated data from multiple exposures (the output of stage 2) into a single rectified (distortion corrected) product, e.g., combining dithers, and/or producing a mosaic; (2) the spectroscopic routines combine multiple images from stage 2 (e.g., a dither/nod pattern) into a single combined two- or three-dimensional spectrum or data cube, and also produce a combined one-dimensional spectrum; (3) the coronagraphic routines produce PSF-subtracted, resampled, combined images from MIRI Lyot and 4QPM exposures; and (4) the time-series routines produce calibrated time-series photometry or spectra from MIRI LRS slitless observations.

---

[34] at https://jwst-docs.stsci.edu/jwst-mid-infrared-instrument/miri-features-and-caveats
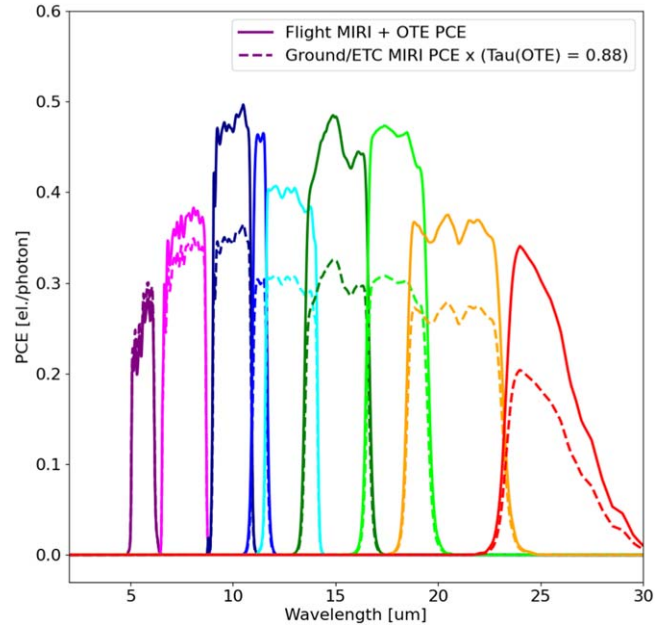

Figure 15. The end-to-end photon conversion efficiency of the Webb Optical Telescope Element (OTE) plus MIRI imager filters. On-ground estimates are plotted as dotted lines, where we assume a flat OTE transmission of 0.88. Flight measurements are plotted as solid lines, and are seen to exceed the ground estimates for all filters.

7. Realized Sensitivity

Pre-launch estimates for the sensitivity of MIRI were provided in Glasse et al. (2015), which discusses the assumptions and methodology that went into predicting MIRI's on-orbit signal-to-noise ratio (S/N) and saturation limits. In short, the aim has been to approach as closely as possible to the sensitivity limit imposed by the Poissonian photon noise floor on the background spectrum due to the sky and, at wavelengths longer than about 15 μm, the thermal emission from the observatory itself. In Glasse et al. (2015), the background was taken from the model results in Lightsey & Wei (2012), with a nominal "low background" case represented as a sum of six Planck spectra, with a seventh graybody spectrum added to model a "high" background case.

The definitive reference for flight-calibrated Webb instrument sensitivities and dynamic range is now the ETC (Pontoppidan et al. 2016), the tool used by observers to plan their observations. The pre-launch S/N predictions of the ETC were reconciled with Glasse et al. (2015); but during commissioning, observations of photometric standard stars allowed us to update the ETC model to reproduce the measured flight performance. Specifically, the photometric calibration observations were used to update the instrument throughput profiles, which we refer to as the photon conversion efficiency (PCE) with units of detected electrons per incident photon.

Figures 15–17 plot the PCEs adjusted to the throughputs measured in flight (solid lines) compared to their ground
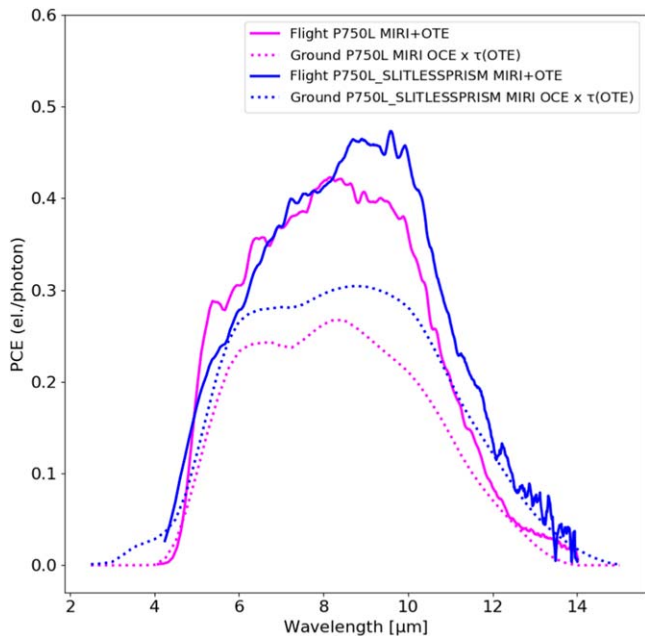
Figure 16. End-to-end photon conversion efficiency of the Webb OTE plus MIRI LRS. See the text for details.
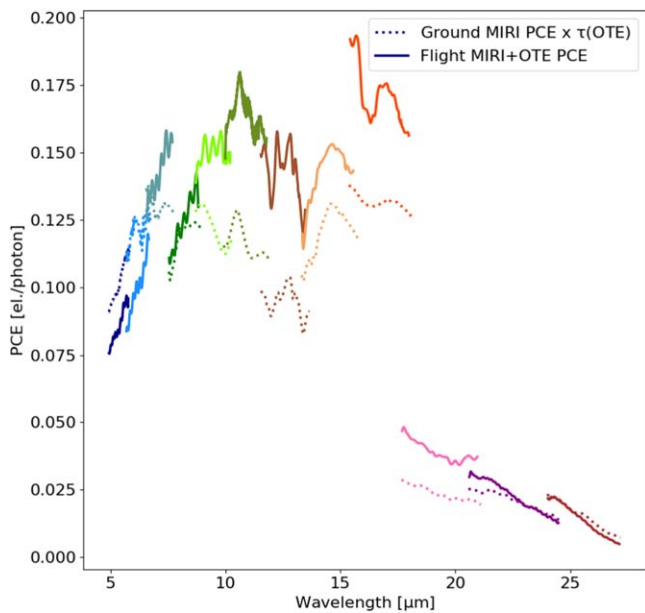

Figure 17. End-to-end photon conversion efficiency of the Webb OTE plus MIRI MRS. See the text for details.

estimated profiles (dotted lines), which were determined from a combination of subcomponent measurements (filter profiles, detector quantum efficiencies, etc.) and model estimates (beginning of life contamination, antireflection (AR) coating performance, etc.). In general, the flight measured PCEs are higher than the ground estimates, where some of this discrepancy may be explained by noting that the ground PCEs included a factor of 0.8 to account for "beginning of life" contamination, which may be a significant overestimate of the transmission losses of the OTE and MIRI optics at this stage of the mission.

For the imager filters, Figure 15 shows a systematic increase in PCE with wavelength compared to the ground prediction, which is not yet well understood. For the LRS, Figure 16 shows the flight PCE, which, as for the imager, is somewhat higher than the pre-flight predictions for both the slitted and slitless modes. We note that the effect of the blocking filter that is bonded to the LRS is apparent in the flight PCE curves as the steeply falling edge to the slitted profile around 4.7 μm, and the overall slight drop in transmission relative to the slitless mode between 8 and 13 μm. The MRS PCE curves shown in Figure 17 show a similar increase in the flight PCEs with wavelength, compared to the ground estimate, at least for channels 1, 2, and 3 (i.e., short of 17.5 μm).

We expect the sensitivity to improve with the square root of any increase in PCE for all but the brightest targets (where flat-fielding and other systematic errors become important), and this is what was seen during commissioning, where, for the imager and MRS flight, measured S/Ns were seen to be typically 10%–20% better than predicted by the pre-flight ETC.

Overall, the MIRI modes have substantially better sensitivity than was predicted in the pre-launch ETC used to plan science observations. This result is due to higher science instrument throughput, a sharper PSF, and cleaner-than-budgeted mirrors for both the telescope and MIRI. It also demonstrates that the observatory background on orbit (Rigby et al. 2023) is sufficiently close to the modeled spectrum that any differences do not have a significant impact on the delivered sensitivity.

8. Conclusion

A broad overview of the in-flight performance of MIRI has been provided, which provides imaging, coronagraphy, and spectroscopy to extend the reach of JWST to 28.5 μm. Commissioning has proven all MIRI functions to perform somewhat better than expected pre-launch and that the instrument has the sensitivity, image quality, spectral resolution and precision, and wavelength range to transform astrophysics at mid-infrared wavelengths. With the ability to provide ultradeep imaging in nine photometric bands, coronagraphy with superb sensitivity, high-precision time-series measurements, and both low- and moderate-resolution spectroscopy, MIRI will enable key breakthroughs in our understanding of galaxies, stars, and planetary systems from our local neighborhood to the distant universe.

ORCID iDs

Gillian S. Wright https://orcid.org/0000-0001-7416-7936
George H. Rieke https://orcid.org/0000-0003-2303-6519
Alistair Glasse https://orcid.org/0000-0002-2041-2462
Michael Ressler https://orcid.org/0000-0001-5644-8830
Macarena García Marín https://orcid.org/0000-0003-4801-0489
Jonathan Aguilar https://orcid.org/0000-0003-3184-0873
Stacey Alberts https://orcid.org/0000-0002-8909-8782
Javier Álvarez-Márquez https://orcid.org/0000-0002-7093-1877
Ioannis Argyriou https://orcid.org/0000-0003-2820-1077
Pierre Baudoz https://orcid.org/0000-0002-2711-7116
Anthony Boccaletti https://orcid.org/0000-0001-9353-2724
Patrice Bouchet https://orcid.org/0000-0002-6018-3393
Jeroen Bouwman https://orcid.org/0000-0003-4757-2500
Bernard R. Brandl https://orcid.org/0000-0001-9737-169X
Stacey Bright https://orcid.org/0000-0001-7951-7966
Luis Colina https://orcid.org/0000-0002-9090-4227
Christophe Cossou https://orcid.org/0000-0001-5350-4796
Alain Coulais https://orcid.org/0000-0001-6492-7719
Misty Cracraft https://orcid.org/0000-0002-7698-3002
Daniel Dicken https://orcid.org/0000-0003-0589-5969
Michael Engesser https://orcid.org/0000-0003-0209-674X
Mireya Etxaluze https://orcid.org/0000-0002-5628-1193
Ori D. Fox https://orcid.org/0000-0003-2238-1572
Scott Friedman https://orcid.org/0000-0002-6211-1932
Danny Gasman https://orcid.org/0000-0002-1257-7742
András Gáspár https://orcid.org/0000-0001-8612-3236
Vincent Geers https://orcid.org/0000-0003-2692-8926
Adrian Michael Glauser https://orcid.org/0000-0001-9250-1547
Karl D. Gordon https://orcid.org/0000-0001-5340-6774
Thomas Greene https://orcid.org/0000-0002-8963-8056
Thomas R. Greve https://orcid.org/0000-0002-2554-1837
Manuel Güdel https://orcid.org/0000-0001-9818-0588
Pierre Guillard https://orcid.org/0000-0002-2421-1350

Thomas Henning ⬥ https://orcid.org/0000-0002-1493-300X
Dean Hines ⬥ https://orcid.org/0000-0003-4653-6161
Bryan Holler ⬥ https://orcid.org/0000-0002-6117-0164
Örs Hunor Detre ⬥ https://orcid.org/0000-0003-0585-4219
Olivia C. Jones ⬥ https://orcid.org/0000-0003-4870-5547
Kay Justtanont ⬥ https://orcid.org/0000-0003-1689-9201
Patrick Kavanagh ⬥ https://orcid.org/0000-0001-6872-2358
Sarah Kendrew ⬥ https://orcid.org/0000-0002-7612-0469
Pamela Klaassen ⬥ https://orcid.org/0000-0001-9443-0463
Alvaro Labiano ⬥ https://orcid.org/0000-0002-0690-8824
Kirsten Larson ⬥ https://orcid.org/0000-0003-3917-6460
David Law ⬥ https://orcid.org/0000-0002-9402-186X
Mattia Libralato ⬥ https://orcid.org/0000-0001-9673-7397
Jose Lorenzo Alverez ⬥ https://orcid.org/0000-0002-6845-993X
Margaret Meixner ⬥ https://orcid.org/0000-0002-0522-3743
Omnarayani Nayak ⬥ https://orcid.org/0000-0001-6576-6339
Bryony Nickson ⬥ https://orcid.org/0000-0002-9915-1372
Alberto Noriega-Crespo ⬥ https://orcid.org/0000-0002-6296-8960
Göran Östlin ⬥ https://orcid.org/0000-0002-3005-1349
Polychronis Patapis ⬥ https://orcid.org/0000-0001-8718-3732
Tom Ray ⬥ https://orcid.org/0000-0002-2110-1068
Pierre Royer ⬥ https://orcid.org/0000-0001-9341-2546
Piyal Samara-Ratna ⬥ https://orcid.org/0000-0002-7332-2866
Beth A. Sargent ⬥ https://orcid.org/0000-0001-9855-8261
Silvia Scheithauer ⬥ https://orcid.org/0000-0003-4559-0721
Bryan Shaughnessy ⬥ https://orcid.org/0000-0001-6493-0029
Irene Shivaei ⬥ https://orcid.org/0000-0003-4702-7561
G. C. Sloan ⬥ https://orcid.org/0000-0003-4520-1044
Tea Temim ⬥ https://orcid.org/0000-0001-7380-3144
Ewine F. van Dishoeck ⬥ https://orcid.org/0000-0001-7591-1907
Bart Vandenbussche ⬥ https://orcid.org/0000-0002-1368-3109
Schuyler Wolff ⬥ https://orcid.org/0000-0002-9977-8255

References

Amiaux, J., Alouadi, F., Augueres, J. L., et al. 2008, Proc. SPIE, 7010, 70100U
Argyriou, I., Rieke, G. H., Ressler, M. E., Gáspár, A., & Vandenbussche, B. 2021, Proc. SPIE, 11454, 114541P
Argyriou, I., Wells, M., Glasse, A., et al. 2020, A&A, 641, A150
Banks, K., Larson, M., Aymergenc, C., & Zhang, B. 2008, Proc. SPIE, 7017, 70170
Baudoz, P., Boccaletti, A., Riaud, P., et al. 2006, PASP, 118, 765
Bely, P. Y., Bolton, J. F., Neeck, S. P., & Tulkoff, P. J. 1987, Proc. SPIE, 751, 29
Boccaletti, A., Cossou, C., Baudoz, P., et al. 2022, A&A, 667, A165
Boccaletti, A., Lagage, P.-O., Baudoz, P., et al. 2015, PASP, 127, 633
Bouchet, P., García-Marín, M., Lagage, P.-O., et al. 2015, PASP, 127, 612
Bouchet, P., Gastaud, R., Lagage, P.-O., et al. 2022, Proc. SPIE, 12180, 121800Z
Bouwman, J., Kendrew, S., Greene, T. P., et al. 2023, PASP, submitted
Bright, S. N., Gordon, K. D., Chen, C. H., et al. 2017, in AIP 512 Astronomical Data Analysis Software and Systems XXV, ed. N. P. F. Lorente, K. Shortridge, & R. Wayth (Melville, NY: AIP), 371

Bright, S. N., Ressler, M. E., Alberts, S., et al. 2016, Proc. SPIE, 99045, 990441
Dicken, D., Rieke, G. H., Ressler, M. E., et al. 2022, Proc. SPIE, 12180, 121802R
Dole, H., Rieke, G. H., Lagache, G., et al. 2004, ApJS, 154, 93
Dressler, A., Brown, R. A., Davidsen, A. F., et al. 1996, HST and Beyond (Washington, D.C: Association of Universities for Research in Astronomy)
Durand, D., Adachi, D., Harvey, D., et al. 2009, Cryocoolers 15 (Boulder, CO: ICC Press)
Fischer, S., Moratschke, D., Straubmeier, C., et al. 2008, Proc. SPIE, 7010, 70103K
Gáspár, A., Rieke, G. H., Guillard, P., et al. 2021, PASP, 133, 014504
Glasse, A., Rieke, G. H., Bauwens, E., et al. 2015, PASP, 127, 686
Glasse, A. C. H., Lee, D., Samara-Ratna, P., & Rieke, G. H. 2020, Proc. SPIE, 11443, 114434D
Glauser, A. M., Glasse, A., Morrison, J. E., et al. 2010, Proc. SPIE, 7731, 77313K
Gordon, K. D., Bohlin, R., Sloan, G. C., et al. 2022, AJ, 163, 267
Gordon, K. D., Chen, C. H., Anderson, R. E., et al. 2015, PASP, 127, 696
Hagan, J. B., Rieke, G. H., Fox, O. D., et al. 2021, PASP, 133, 114503
Hollenbach, D., & McKee, C. F. 1989, ApJ, 342, 306
Hora, J. L., Fazio, G. G., Allen, L. E., et al. 2004, Proc. SPIE, 5487, 77
Illingworth, G. 2016, STScI Newsletter, 33, 6
Kendrew, S., Dicken, D., Bouwman, J., et al. 2018, Proc. SPIE, 10698, 106983U
Kendrew, S., Scheithauer, S., Bouchet, P., et al. 2015, PASP, 127, 623
Kendrew, S., Scheithauer, S., Bouchet, P., et al. 2016, Proc. SPIE, 9904, 990443
Kimble, R. A., Vila, M. B., Van Campen, J. M., et al. 2016, Proc. SPIE, 9904, 990408
Klaassen, P. D., Geers, V. C., Beard, S. M., et al. 2021, MNRAS, 500, 2813
Krause, O., Birkmann, S., Blumchen, T., et al. 2008, Proc. SPIE, 7018, 701824
Kroes, G., Oudenhuysen, A., de Haan, M., et al. 2010, Proc. SPIE, 7731, 77313S
Labiano, A., Argyriou, I., Álvarez-Márquez, J., et al. 2021, A&A, 656, A57
Labiano, A., Azzollini, R., Bailey, J., et al. 2016, Proc. SPIE, 9910, 99102W
Lajoie, C.-P., Soummer, R., Hines, D. C., & Rieke, G. H. 2014, Proc. SPIE, 9143, 91433R
Lightsey, P. A., & Wei, Z. 2012, Proc. SPIE, 8442, 84423B–1
Mather, J., et al. 2023, PASP, submitted
McKee, C. F. G., Taylor, J. H., et al. 2001, Astronomy and Astrophysics in the New Millennium: Panel on Ultraviolet, Optical and Infrared Astronomy from space, National Academies of Sciences, Engineering, and Medicine (Washington, DC: The National Academies Press)
Morrison, J. E., Dicken, D., Argyriou, I., et al. 2023, PASP, submitted
Penanen, K., Breda, D., Moore, B., et al. 2020, Cryocoolers, Vol. 22 (Boulder, CO: ICC Press)
Petach, M., Michaelian, M., & Nguyen, T. 2018, IOP Conf. Ser.: Materials Science and Engineering, 755, 012018
Petroff, M. D., & Stapelbroek, M. G. 1984, Proc. of the Meeting of the Specialty Group on Infrared Detectors, IRIA-IRIS, Vol. 2 (Ann Arbour, MI: ERIM)
Pontoppidan, K. M., Pickering, T. E., Laidler, V. G., et al. 2016, Proc. SPIE, 9910, 991016
Renouf, I., & Wright, D. 2006, MIRI-DD-00001-AEU, Mid-Infrared Instrument (MIRI), OBA Design Description, DRL SI-01, MIRI European Consortium
Ressler, M. E., Sukhatme, K. G., Franklin, B. R., et al. 2015, PASP, 127, 675
Ressler, M. E., Cho, H., Lee, R. A. M., et al. 2008, Proc. SPIE, 7021, 19
Rieke, G. H., Ressler, M. E., Morrison, J. E., et al. 2015, PASP, 127, 665
Rigby, J., Lightsey, P. A., García Marín, M., et al. 2023, PASP, 135, 048002
Ross, R. G., Boyle, R. F., & Kittel, P. 2004, in AIP Conf. Ser. 710 Advances in Cryogenic Engineering: Transactions of the Cryogenic Engineering Conference—CEC, ed. J. Waynert et al. (Melville, NY: AIP), 1197
Rossi, L., Jamoye, J.-F., Renotte, E., et al. 2008, Proc. SPIE, 7018, 701823
Rouan, D., Baudrand, J., Boccaletti, A., et al. 2007, C.R. Physique, 8, 298
Shaughnessy, B. M. 2012, in Thermal Design and Testing of the Mid-Infrared Instrument (MIRI) Optics Module, Int. Conf. Environmental Systems (ICES) (Red Hook, NY: Curran Associates)

Space Telescope Science Institute 2023, https://jwst-pipeline.readthedocs.io/en/latest/jwst/user_documentation/introduction.html

Spinoglio, L., & Malkan, M. A. 1992, ApJ, 399, 504

Sukhatme, K. G., Thelen, M. P., Cho, H., & Ressler, M. E. 2008, Proc. SPIE, 7021, 70210N

van Dishoeck, E. F. 2004, ARA&A, 42, 119

Wells, M., Pel, J.-W., Glasse, A., et al. 2015, PASP, 127, 646

Wright, G. S., Wright, D., Goodson, G. B., et al. 2015, PASP, 127, 595

Wu, J., Forrest, W. J., Pipher, J. L., Lum, N., & Hoffman, A. 1997, RScI, 68, 3566

Yu, J. 2010, Charge Injection and Clock Feedthrough, Master's thesis, San Jose State University, available at, https://scholarworks.sjsu.edu/etd_theses/index.15.html